Open access • Journal Article • DOI:10.1021/ACS.CHEMMATER.8B03669

Sulfur poisoning recovery on a solid oxide fuel cell anode material through reversible segregation of nickel — Source link

Patrick Steiger, Patrick Steiger, Dariusz Burnat, Hossein Madi ...+7 more authors

Institutions: École Polytechnique Fédérale de Lausanne, Paul Scherrer Institute, Zürcher Fachhochschule, Winterthur Museum, Garden and Library

Published on: 06 Jan 2019 - Chemistry of Materials (American Chemical Society)

Topics: Solid oxide fuel cell, Oxide, Anode, Mixed oxide and Nickel

CHEMISTRY OF MATERIALS

Article

Sulfur poisoning recovery on a SOFC anode material through reversible segregation of nickel

Patrick Steiger, Dariusz Burnat, Hossein Madi, Andreas Mai, Lorenz Holzer, Jan Van Herle, Oliver Kröcher, Andre Heel, and Davide Ferri

Chem. Mater., **Just Accepted Manuscript** • DOI: 10.1021/acs.chemmater.8b03669 • Publication Date (Web): 06 Jan 2019

Just Accepted

ACS Publications

is published by the American Chemical Society. 1155 Sixteenth Street N.W., Washington, DC 20036

Sulfur poisoning recovery on a SOFC anode material through reversible segregation of nickel

Patrick Steiger[a,b], Dariusz Burnat[c], Hossein Madi[d], Andreas Mai[e], Lorenz Holzer[f], Jan Van Herle[d], Oliver Kröcher[a,b], Andre Heel[c], and Davide Ferri[a]*

[a] Paul Scherrer Institut, CH-5232 Villigen, Switzerland

[b] École polytechnique fédérale de Lausanne (EFPL), Institute of Chemical Sciences and Engineering, CH-1015 Lausanne, Switzerland

[c] Zurich University of Applied Sciences, IMPE – Institute for Materials and Process Engineering, CH-8400 Winterthur, Switzerland

[d] École polytechnique fédérale de Lausanne (EFPL), Institute of Mechanical Engineering, CH-1951 Sion, Switzerland

[e] HEXIS AG, CH-8404 Winterthur Switzerland

[f] Zurich University of Applied Sciences, ICP – Institute of Computational Physics, CH-8400 Winterthur, Switzerland

* Corresponding author
e-mail: davide.ferri@psi.ch
Phone: +41 56 310 27 81

Abstract

The perovskite-type mixed oxide $La_{0.3}Sr_{0.55}Ti_{0.95}Ni_{0.05}O_{3-\delta}$ (LSTN) is demonstrated to exhibit the remarkable property of structural regeneration, where Ni can be reversibly exsoluted from the host perovskite lattice resulting in a regenerable Ni catalyst for solid oxide fuel cell anode applications. Results of catalytic tests for the water gas shift reaction and electrochemical investigations on a button sized fuel cell demonstrate the redox stability of LSTN, its potential application in solid oxide fuel cells and its ability to recover catalytic activity completely after sulfur poisoning. Nickel segregation was characterized and quantified on powder samples by means of electron microscopy, X-ray diffraction, X-ray absorption spectroscopy as well as temperature programmed reduction – reoxidation cycles. Catalyst stability was much improved compared to impregnated $Ni/La_{0.3}Sr_{0.55}TiO_{3-\delta}$ and $Ni/Y_{0.08}Zr_{0.92}O_2$ anode materials. A full cell was tested under both open circuit voltage and polarized conditions showing a stable cell voltage over redox cycles as well as periods of reverse potential and current overload. The area specific resistance of the anode layer was as low as 0.58 Ωcm^2 at 850°C. This allows LSTN to be applied in redox stable solid oxide fuel cell anodes and reversible segregation of Ni to be exploited for fast recovery from sulfur poisoning.

Introduction

Modern society relies on the development of highly efficient and stable power sources ideally capable of using variable fuel sources to meet the ever increasing electricity demand.[1-2] Solid oxide fuel cells (SOFC) offer exceptionally high efficiency for chemical to electric power conversion with high fuel flexibility.[3-5] Unlike other types of fuel cells their high operating temperatures allow for hydrocarbon fuels from various sources to be directly used via internal reforming reactions[6-7] producing hydrogen and carbon monoxide mixture fuels. This is a major advantage over polymer electrolyte fuel cells (PEM), which rely on highly pure hydrogen as fuel gas.[8] Internal reforming occurs at the SOFC anode, Ni metal catalyzes this reaction as well as the important hydrogen oxidation reaction ($H_2 + ½O_2 \rightarrow H_2O$, HOR) and the water gas shift reaction ($CO+H_2O \rightarrow CO_2+H_2$, WGS), which produces additional H_2 fuel from residual steam originating from reforming or water generated through HOR.[9] Besides catalytic activity, the anode material has to provide also both, high ionic and electronic conductivity for the electrochemical oxidation of the fuel gas and for current collection, respectively. For a long time $Ni/Y_{0.08}Zr_{0.92}O_2$ (Ni/YSZ) cermets have been the state-of-the-art anode material offering both high catalytic activity (due to addition of a considerable amount of Ni, ca. 50 wt%) as well as good conductivity for both electrons and oxygen anions provided by the percolating Ni and YSZ phases, respectively.[10-12] However, their poor redox stability is regarded as a major disadvantage besides their susceptibility to poisoning by sulfur.[13-14] Sulfur contaminants are commonly present in fuel gas as they are used as odorants for natural gas or may be present in large quantities in biogenic fuels. At low concentrations sulfur species are known to strongly adsorb on the Ni surface thus deactivating the metal catalyst.[15-18] High sulfur concentrations may induce the formation of sulfur compounds (e.g. NiS, Ni_3S_2 and Ni_7S_6) that permanently degrade Ni containing SOFC anodes not only with respect to catalytic activity for hydrogen oxidation but especially for WGS.[17-18] Sulfur was also

observed to promote the migration of Ni, thus decreasing the degree of Ni percolation within the anode and reducing electronic conductivity.[19]

For these reasons much attention is currently drawn to the development of novel SOFC anode materials capable to offer the required electrochemical performance and stability in sulfur containing feeds. Other beneficial properties such as redox stability could be potentially exploited as it would allow operating the cell in electrolysis mode but also regenerating a deactivated anode from sulfur poisoning and/or coke deposits, which may have formed during internal reforming of hydrocarbons. Reduction of overall Ni content is essential to achieve redox stability. Besides the coarsening of the Ni phase, the oxidation of Ni and consequential volume expansion of the Ni phase may lead to electrode or electrolyte cracking.[13-14, 20-22] Perovskite-type oxides (ABO_3) are regarded as good candidates to replace high Ni content anode cermets with the aim of increasing anode durability.[23-25] Their inherent structural stability allows for a large number of elements to be incorporated at various stoichiometries within their lattice and thus ultimately for the tailoring of both electronic and ionic conductivities besides catalytic properties. Among others, lanthanum doped strontium titanates have attracted attention since they are temperature and redox stable and offer the necessary conductivities required for SOFC electrode applications.[23] Nickel can still be added for its catalytic activity and is deposited on the perovskite backbone in the form of nanoparticles usually by impregnation.[25-27]

In more recent years direct Ni exsolution from the perovskite lattice through selective reduction has been shown to produce particles with enhanced sintering and coking resistance.[28-32] Exsolution from perovskite-type mixed oxides is achieved by partially substituting the B-site elements of a redox stable perovskite host lattice by Ni and subjecting these materials to a reductive environment. This causes the dispersed Ni within the perovskite to reduce and segregate forming well dispersed particles on the perovskite surface, while the rest of the perovskite remains intact and structurally stable. Segregated Ni particles show much higher particle-support interactions compared to Ni particles deposited through

conventional support impregnation methods, as they remain partially embedded in the surface of the perovskite material, which pins them in place.[28] Some perovskite-type oxides have also been shown to exhibit the remarkable property of structural self-regeneration, i.e. the reversible reincorporation of such particles into the perovskite lattice. This capability was shown to depend on both composition of the host perovskite as well as on the regeneration conditions (i.e. oxygen partial pressure and temperature) and has been demonstrated for a variety of Pt group metals for exhaust gas after treatment catalysts and recently for Fe and Co.[33-37] Ni has also been shown to segregate and reincorporate reversibly during simple redox cycles from $LaFe_{1-x}Ni_xO_{3\pm\delta}$ perovskite-type oxides[38-39] and more recently $La_{0.7}Sr_{0.3}Cr_{1-x}Ni_xO_{3-\delta}$.[40] Exploitation of this effect produced highly redox stable catalysts, enabling the preservation of metal particle size and thus activity over repeated redox cycles.

The objective of this work was to demonstrate that, if a material with such a property was applied as a SOFC anode, anode reoxidation at high temperatures could be utilized to remove poisoning (such as H_2S) from its surface through simple reoxidation as well as allowing the cell to be operated in electrolysis mode. We demonstrate that $La_{0.3}Sr_{0.55}Ti_{0.95}Ni_{0.05}O_{3-\delta}$ exhibits all the properties required for operation as SOFC anode and verify the advantage of structural self-regeneration. This property can indeed be exploited on this perovskite-type host to restore the catalytic activity of Ni towards the water gas shift reaction after sulfur poisoning and to produce redox stable SOFCs.

Experimental details

Mixed metal oxides with nominal composition $La_{0.3}Sr_{0.55}TiO_{3-\delta}$ (LST) and $La_{0.3}Sr_{0.55}Ti_{0.95}Ni_{0.05}O_{3-\delta}$ (LSTN) were synthesized using a citrate-gel method described including a final calcination step at 960°C for 6 h.[30] After calcination the powders are referred to as "calcined". Nickel impregnated LST (Ni/LST) was prepared by wet impregnation of the as calcined LST perovskite with an aqueous solution of $Ni(NO_3)_2 \cdot 6H_2O$ (pro analysis, Merck). Drying at 90°C overnight was followed by calcination in air at 500°C for 2 h. Furthermore, $Y_{0.08}Zr_{0.92}O_2$ was impregnated with an aqueous solution of $Ni(NO_3)_2 \cdot 6H_2O$ according to the same procedure to obtain 60 wt% NiO/YSZ (calculated 50 vol% Ni/YSZ) representing a standard solid oxide fuel cell anode material. In order to characterize the redox stability and the catalytic activity towards the water gas shift (WGS) reaction of these materials, aliquots of the powders received reductive and oxidative pretreatments or combinations thereof. If not otherwise stated all pretreatments were conducted at 800°C. Reduction was carried out in 10 vol% H_2/Ar, whereas oxidation was conducted in synthetic air (20 vol% O_2/N_2) in a tubular quartz reactor.

The specific surface area (SSA) of the calcined powders was calculated from N_2-adsorption isotherms at -196°C according to the Brunauer-Emmet-Teller (BET) model. Adsorption data was acquired using a Quantachrome Autosorb I instrument. Prior to SSA determination the samples were treated under vacuum at 300°C for 2 h.

The phase composition and crystal structure of calcined, reduced (10 vol% H_2, 800°C, 15 h) and reoxidised powders (20 vol% O_2, 800°C, 2 h) were analyzed by ex situ powder X-ray diffraction (XRD) using a Bruker D8 Advance diffractometer equipped with Ni-filtered Cu radiation, variable slits and an energy sensitive line detector (LynxEye). Diffractograms were collected between 15°-80° 2θ with an acquisition time of 4 s and a step size of $\Delta 2\theta = 0.03°$.

Temperature programmed reduction (TPR) experiments were conducted using a bench top TPDRO-1100 (ThermoElectron) instrument equipped with mass flow controllers and a thermal conductivity detector. The samples (100 mg) were loaded into the quartz reactor tube and heated to 500°C under constant flow of 20 vol% O_2 before cooling to room temperature. TPRs were recorded in 10 vol% H_2/Ar (20 mLmin^{-1} at STP) and at a heating rate of 5°Cmin^{-1}. The reoxidation temperature at which Ni is reversibly reincorporated into the perovskite lattice was estimated by TPR redox experiments. A TPR profile was recorded on the calcined sample up to 800°C followed by isothermal reduction for 1 h at the same temperature. The sample was then cooled in Ar to room temperature (25°C) before reoxidation at 700°C in 20 vol% O_2/N_2 for 2 h. The sample was again cooled in Ar to 25°C before starting the second TPR on the now reoxidised material. Such TPR-reduction-reoxidation-TPR cycles were repeated five times with increasing reoxidation temperature (700°C, 750°C, 800°C, 850°C and 900°C). The heating rate during reoxidation and cooling after all experiments was 10°Cmin^{-1}.

Nickel K-edge (8.333 keV) X-ray absorption spectra were acquired ex situ on pelletized samples in fluorescence mode at the X10DA (SuperXAS) beamline of the Swiss Synchrotron Light Source (SLS, Villigen, Switzerland) using a 5 element SD detector. The required X-ray energies were scanned using a Si(111) monochromator. The Demeter software package (version 0.9.24)[41] was used to reduce and model all data. The radial distribution function (R) was obtained by Fourier transforming k^3-weighted k-functions typically in the range of 3.0 - 12.0 Å^{-1} using a Hanning window function. Fitting of bond distances was generally performed in the range of 1.0-4.0 Å. NiO (99.99% trace metals basis, Sigma) and Ni foil references were measured in transmission mode using ionization chamber detectors.

Linear combination fitting (LCF) of X-ray absorption near edge structure (XANES) spectra was performed in the spectral range -20 eV < E_0 < 30 eV around the absorption edge to quantify the fraction of each Ni species present in the samples. Reference compounds for each fit included Ni-foil,

NiO and calcined $La_{0.3}Sr_{0.55}Ti_{0.95}Ni_{0.05}O_{3\pm\delta}$ representing Ni^{n+}_{oct} (n>2) in the perovskite coordination environment.

X-ray fluorescence was collected ex situ on pretreated and pelletized samples at the Phoenix beamline at SLS. A 4-element Si drift diode array was used to collect fluorescent radiation at am incident X-ray energy of 2600 eV.

Changes in the microstructure of the samples as a result of repeated redox cycles were studied using scanning electron microscopy (field emission SEM, Zeiss ULTRA 55). The samples were analyzed using a 5 keV electron beam and the in-lens secondary electron detector at a working distance of 1.8 mm. Typical magnifications in the range of 50'000-100,000 allowed the analysis of Ni particles of ca. 5-10 nm.

Scanning transmission electron microscopy (STEM) images were acquired using an analytical TEM (FEI Talos F200X) equipped with a Super-X EDX system (windowless) and a high angle annular dark field (HAADF) detector. The accelerating voltage was set to 200 kV. EDX maps (512 x 512 pixels) were acquired with a resolution of 7 nm.

Catalytic activity tests towards the water gas shift reaction (WGS) were carried out with a homemade test setup in a quartz reactor of plug flow geometry (6 mm ID). Mass flow controllers were used to dose the reactant gases and a thermocouple placed in the middle of the catalyst bed was used to determine catalyst bed temperature. To avoid back pressure all calcined powders were pelletized (4 MPa), crushed in an agate mortar and sieved to 100-150 µm before use. The catalyst (100 mg) was diluted with cordierite powder (100 mg, 75-100 µm) to achieve a thoroughly mixed catalyst bed of 10 mm in length. The reactant gas containing 15 vol% CO, 15 vol% H_2O, 7.5 vol% H_2 (rest Ar) was fed at a total flow rate of 50 $mLmin^{-1}$ at STP resulting in a weight hourly space velocity (WHGS) of 30,000 $mLg^{-1}h^{-1}$. Catalytic tests were conducted on pre-reduced samples (20 vol% H_2, 800°C, 1 h). The

experiment was started at 800°C under reaction conditions after the catalyst was left to equilibrate for 10 min before cooling to 300°C at 5 °Cmin^{-1}. All stainless steel gas lines were heated to 120°C to avoid condensation. Compositional analysis of the exhaust gas was performed using a quadrupole mass spectrometer (Pfeiffer OmniStar GSD 320) equipped with a heated stainless steel capillary. CO conversion (C_{CO}) was determined according to eq. 1

$$C_{CO}\,[\%] = 100 \cdot \frac{[CO]_{in} - [CO]_{out}}{[CO]_{in}} \tag{1}$$

where $[CO]_{in}$ and $[CO]_{out}$ are the initial and final CO concentrations, respectively.

Equilibrium conversions were calculated from the following expression (eq. 2) for the WGS equilibrium constant K_{eq}[42]

$$\log K_{eq} = \frac{5693.5}{T} + 1.077 \ln T + 5.44 * 10^{-4} T - 1.125 * 10^{-7} T^2 - \left(\frac{49170}{T^2}\right) - 13.148 \tag{2}$$

and the relationship

$$K_{eq} \cong \frac{[CO_2] * [H_2]}{[CO] * [H_2O]} \tag{3}$$

where $[CO_2]$, $[H_2]$, [CO] and $[H_2O]$ are the concentrations of the corresponding gases at equilibrium.

The effect of sulfur poisoning was assessed on pre-reduced LSTN (20 vol% H_2/Ar, 800°C, 1 h) after eight redox cycles. The material was subjected to the water gas shift reaction mixture additionally containing 50 ppm H_2S at 800°C for 2 h before cooling in Ar. The water gas shift activity of the poisoned catalyst was then obtained in identical tests to those on the non-poisoned material. Catalyst regeneration was conducted through two consecutive redox cycles at 800°C (1 h reduction followed by 2 h reoxidation).

The preliminary tests of full solid oxide cells based on pure LSTN anodes exhibited a high polarization resistance due to the low ionic conductivity of the LSTN anode layer because of the short length of triple phase boundaries at the interphase with the electrolyte.[43-44] Hence, electrochemical tests were conducted on composite electrodes with high LSTN content in a full cell design. LSTN powders were mixed with ionically conductive gadolinium cerium oxide ($Ce_{0.9}Gd_{0.1}O_2$, CGO), dispersed in terpene alcohol (mixture of isomers, anhydrous, Fluka) and homogenized by planetary milling as described elsewhere.[45] Screen-printable inks with 60 vol% LSTN and 40 vol% CGO and $La_{0.2}Sr_{0.8}MnO_3$-$Y_{0.15}Zr_{0.85}O_2$ (LSM-YSZ) cathodes (50:50 vol%) were printed onto sintered $Sc_{0.12}Zr_{0.88}O_2$ electrolyte (120 µm thickness, non-reactive with titanates) and both electrodes were co-fired at 1150°C for 3 h.[46] Nickel-free LST was printed on top of the active layer of the electrode for current collection and contacted to measurement electrodes by Au and Ni meshes. The prepared cells (active electrode area = 1.44 cm^2) were inserted into the test setup, sealed with a ceramic gasket (Insufliz) and connected to the measuring terminal (Zahner IM6ex). Electrochemical impedance spectroscopy (EIS) and voltammetry were used for characterization. Cells were heated in oxidizing atmosphere at a rate of 3 $^oCmin^{-1}$ and anodes reduced and operated in pure hydrogen (PanGas, 5.0) at a gas flow of 200 $mLmin^{-1}$ at STP. Air was supplied to the cathode with a flow rate of 450 $mLmin^{-1}$ at STP. Cell temperature was measured via the thermoelectric potential of an S-type thermocouple located close to the cell. Anode reoxidation was conducted by 30 min fuel cut-offs at the working temperature of 850°C under open circuit voltage (OCV). The cell was operated in electrolysis mode (-2.0 V) twice for 2 min and once for 2 min under current overload (2.0 Acm^{-2}) to monitor the effects of these treatments on area specific resistance. Impedance spectra were collected in the frequency range between 0.01 Hz and 1 MHz in galvanostatic mode, both under OCV and under polarization when drawing 200 $mAcm^{-2}$. Changes in the impedance spectra were analyzed by Analysis of Differences in Impedance Spectra (ADIS), which shows frequency dependent changes of impedance upon variation of operating conditions.[47]

The differential method (ADIS) is based on the analysis of real parts of impedance spectra:

$$\Delta\delta Z = \left| \left(\frac{\partial Z_{\text{Real}}^{P1}}{\partial \log f} \right) - \left(\frac{\partial Z_{\text{Real}}^{P2}}{\partial \log f} \right) \right| \tag{4}$$

where δZ_{Real}^{P1} and δZ_{Real}^{P2} are differentials of the real impedance part upon the change of one experimental parameter (P1, P2 represent states before and after redox cycling).

3. Discussion

3.1 Nickel reduction and segregation

The individual powder grains of calcined $La_{0.3}Sr_{0.55}Ti_{0.95}Ni_{0.05}O_{3-\delta}$ (LSTN) were composed of individual crystallites forming a porous network as depicted in the scanning electron microscopy (SEM) image in Figure 1-a. All calcined perovskite-type oxide powders showed excellent phase purity and high crystallinity (Figure S1). Table S1 summarizes general powder characterization results including specific surface areas (SSA) and the analysis of X-ray diffraction (XRD) patterns. All sample abbreviations used throughout the discussion are also given in Table S1. The perovskite samples LSTN and LST contained a single cubic perovskite phase (Pm-3m), which was observed and reported also for undoped and stoichiometric $SrTiO_{3\pm\delta}$.[48] No indication of secondary phases (NiO) could be found by SEM on impregnated Ni/$La_{0.3}Sr_{0.55}TiO_{3-\delta}$ (Ni/LST, Figure 1-b) even though NiO reflections (i.e. (200) at $2\theta \approx 43.3°$) could be observed by XRD. Reduction of both LSTN and Ni/LST at 800°C resulted in the display of metallic Ni particles on the surface of the materials. This is less surprising in the case of impregnated Ni/LST where NiO was simply reduced to Ni^0 on the support surface. In LSTN however, formation of the observed particles must have occurred from reduction of Ni from the bulk of the material and segregation to the crystallite surface. The segregation of Ni and the formation of Ni

particles on LSTN can be observed in the STEM image of the sample reduced at 800°C/15 h (Figure 1-c), after which few small particles in the size range of 10 – 30 nm were visible. These features overlap with the areas of increased Ni concentrations obtained from the elemental mapping of Ni (STEM EDX, Figure 1-d). All other elements remained uniformly distributed across the particles and likely remained inside the metal oxide crystallites. Therefore, we consider that segregation of other elements than Ni did not occur.

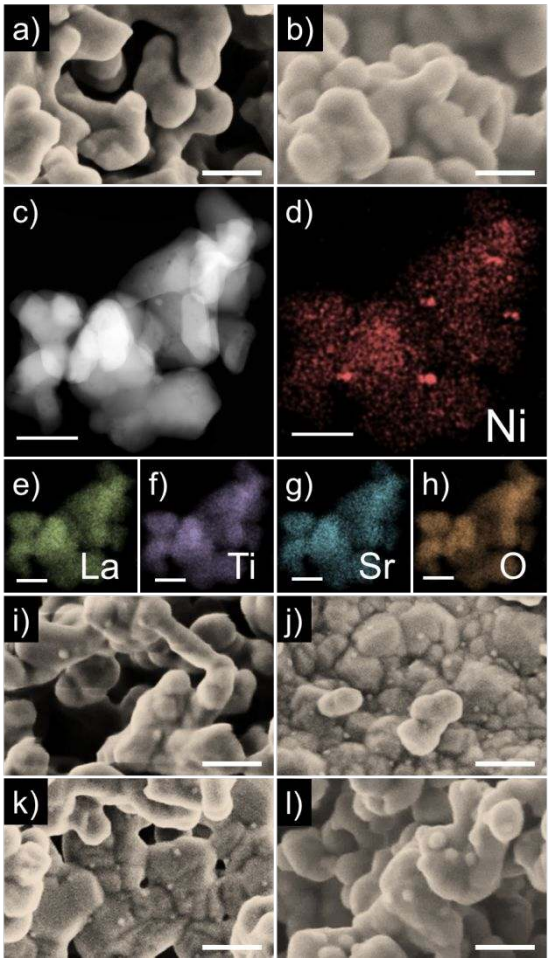

Figure 1. SEM images of a) LSTN and b) Ni/LST after calcination. c) High angle annular dark field TEM image of reduced LSTN (800°C, 10 vol% H_2, 15 h); Elemental maps (STEM-EDX) of same sample region displaying Ni, (d) La, (e) Ti, (f) Sr (g) and O concentrations (h). Scale bars represent 200 nm. SEM images of (i) LSTN and (j) Ni/LST after single reduction (800°C, 10 vol% H_2, 1 h) as well as reduced after eight redox cycles (k) and (l), respectively. Scale bars on SEM images represent 100 nm.

3.2 Self-regenerating property

Inherent material redox stability is decisive for application in a regenerable SOFC anode. Since the intended regeneration from sulfur poisoning involves anode redox cycling, additional catalyst deactivation due to Ni particle growth over the number of redox cycles may strongly limit its functionality. Figure 1 depicts a series of SEM images of LSTN (Figure 1-i and Figure 1-k) and Ni/LST (Figure 1-j and Figure 1-l) after a single reduction step at 800°C and reduced after eight redox cycles. Nickel particles are visible on all images. However, in the case of LSTN the size of these particles did not change significantly over eight redox cycles, whereas clear indications of Ni particle growth can be seen in the case of Ni/LST. After a single reduction step the material displayed numerous small Ni particles (mean size ca. 10 nm), whereas after eight redox cycles most particles had grown to 20-40 nm in size. Therefore, particle growth over redox cycles was indeed an issue on the impregnated Ni/LST, whereas the self-regenerating property of LSTN stabilized Ni particle size over the course of the treatment.

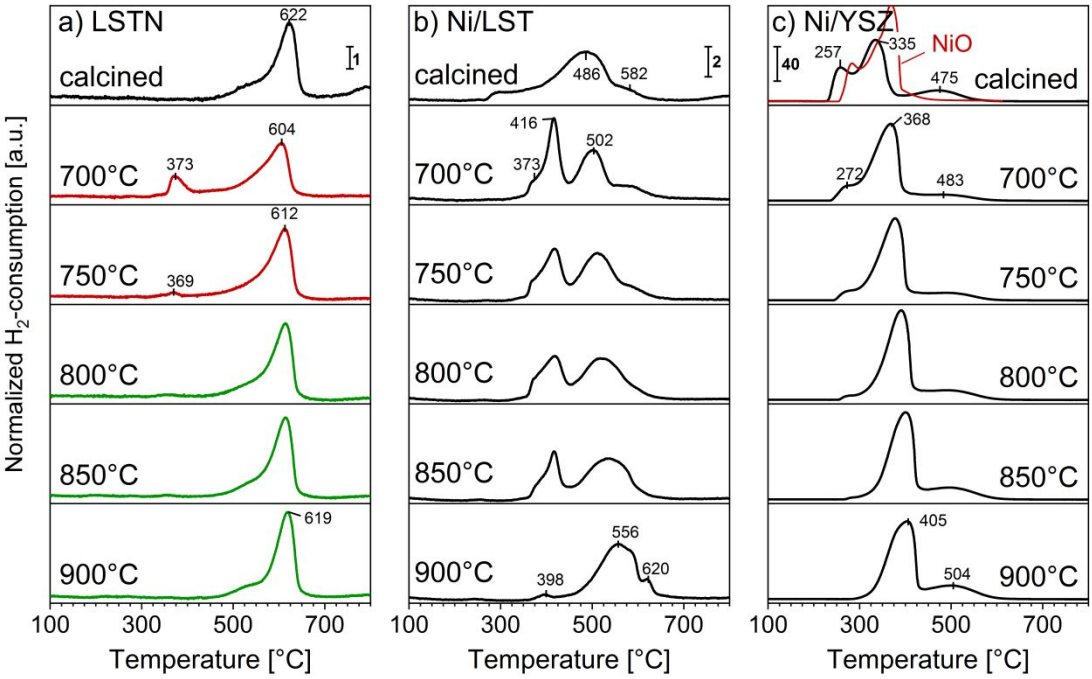

Figure 2. Temperature programmed reduction-reoxidation cycles for (a) LSTN, (b) Ni/LST and (c) Ni/YSZ. Hydrogen consumption values were normalized by the number of moles of sample used. Reoxidised samples were subjected to pre-reduction in 10 vol% H_2 at 800°C for 1 h before reoxidation at the given temperature (20 vol% O_2, 2 h). Reduction profile of NiO reference is depicted in top row of c).

Metal segregation from and reincorporation back into perovskite-type oxide lattices is a temperature dependent process.[49] It is therefore of great interest for practical application to determine the reoxidation temperature at which Ni can be completely reincorporated into the perovskite lattice. This was achieved using a strategy previously applied to investigate Ni reincorporation into $LaFe_{1-x}Ni_xO_{3\pm\delta}$ host lattices.[38] Figure 2 shows the results of H_2-temperature programmed reduction (TPR) – reoxidation cycles on the three Ni catalysts. Similarities in the reduction profiles of calcined Ni/LST (Figure 2-b) and Ni/YSZ (Figure 2-c) were expected since XRD analysis (summarized in Table S1) already indicated the presence of a NiO phase dispersed on both materials. Reduction started below 250°C and appeared to be complete at 630°C. Reduction of calcined Ni/LST peaked at 486°C, whereas

the highest hydrogen consumption of Ni/YSZ occurred at 335°C. In general, the shape and temperature range of the reduction profile of Ni/YSZ was very similar to that obtained on pure NiO powder, which showed maximum rate of reduction at 370°C (Figure 2-c). In marked contrast, H_2-consumption during the TPR of calcined LSTN started at 450°C and peaked at 622°C. The evident differences in the reduction profiles of these materials are due to the different state of Ni - as determined by X-ray absorption spectroscopy (XAS, vide infra in Figure 4) - and distinguish NiO from incorporated Ni species (Ni^{n+}_{oct}). Reduction profiles can therefore be used to determine the state of Ni and to estimate the oxidation temperature necessary to reincorporate Ni into the perovskite lattice.

Figure 2 also shows a series of TPR profiles for each sample after pre-reduction (800°C, 10 vol% H_2/Ar, 1 h) and subsequent reoxidation (T=700, 750, 800, 850 and 900°C, 20 vol% O_2/N_2, 2 h). In the case of LSTN, whenever the reoxidation temperature was not sufficient to reincorporate all Ni into the lattice during the reoxidation a distinctive reduction peak of NiO appeared at ca. 370°C in the subsequent TPR. After reoxidation at T ≥ 800°C this NiO feature disappeared, which indicated full Ni reincorporation into the LSTN lattice.

Ni/LST and Ni/YSZ also showed changes in the reduction profiles from the calcined to the reoxidised materials, which can be attributed predominantly to morphological changes of the NiO phase.[50] The higher reduction temperature of NiO/LST compared to Ni/YSZ was attributed to the close contact between the small amount of Ni and the oxygen providing perovskite surface in Ni/LST. In this case, LST might have acted as an oxygen source to prevent NiO reduction at low temperatures. Nevertheless, from the evolution of the reduction profile shape of the impregnated samples (Ni/LST and Ni/YSZ) it can be assumed that Ni was always present as NiO species after each reoxidation cycle.

Similar TPR redox experiments involving multiple redox cycles at a constant reoxidation temperature of 800°C were also conducted (Figure S2). This temperature is typical of SOFC operation[51] as well as the temperature at which Ni was found to reincorporate into the perovskite lattice in LSTN. The

reduction profile of LSTN showed complete reversibility over all cycles and the temperature range of H_2-consumption remained between 450°C and 650°C with a maximum at 614-627°C. Reversible reduction profiles were also found for Ni-free LST pointing to the intrinsic redox stability of the host perovskite structure. The reduction feature observed for LST was assigned to the loss of oxygen and partial reduction of Ti^{4+} to Ti^{3+}. The two impregnated samples Ni/LST and Ni/YSZ appeared to change significantly after the first reoxidation. Changes were likely due to the low initial calcination temperatures of 500°C after impregnation with the Ni precursor compared to the high reoxidation temperature of 800°C used during the experiment. After the first high temperature reoxidation all samples maintained their reduction profiles in the next redox cycles. Slight peak narrowing was observed over the course of the redox cycles for the two impregnated samples, which has previously been attributed to increased metal oxide crystallinity and can also be taken as an indication of NiO particle growth, hence degeneration of the potential anode material.[52]

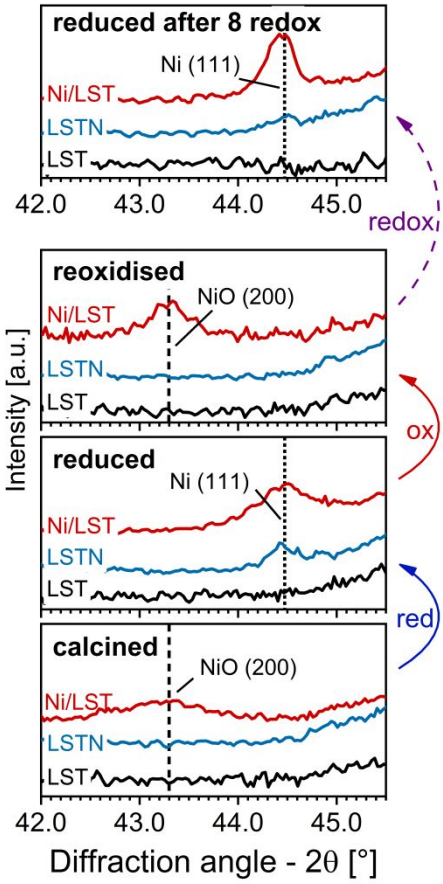

Figure 3. X-ray diffraction patterns of LST (black) LSTN (blue) and Ni/LST (red) in the angular range of 42.0° ≤ 2θ ≤ 46.0° in their calcined state, after reduction (800°C, 10 vol% H_2, 1 h), after reoxidation (800°C, 20 vol% O_2, 2 h) and reduced after eight redox cycles. The position of the NiO (200) reflection at 43.299° and the Ni (111) reflection at 44.473° are indicated with dashed and dotted lines, respectively.

The beneficial consequences of exploiting the smart material concept,[30] i.e. the absence of Ni particle growth on LSTN and the evidence of particle growth on impregnated Ni/LST, can also be visualized by XRD. Figure 3 shows the angular range in 2θ between 42 – 45.5° (including the main (200) reflection of NiO at 43.3° and the (111) reflection of Ni at 44.5°) of LSTN, Ni/LST as well as plain LST for reference purposes over a similar series of redox cycles. Only a broad NiO reflection was

observed on calcined Ni/LST, whereas no NiO reflection was present in LSTN and obviously LST (Figure 3-a). After reduction at 800°C the Ni (111) reflection appeared in both LSTN and Ni/LST (Figure 3-b). This reflection disappeared on LSTN after reoxidation at 800°C, whereas it changed into a strong NiO reflection in the case of Ni/LST. This indicates complete Ni reincorporation in the case of LSTN and the absence of this process in Ni/LST (Figure 3-c). However, XRD may not be sensitive enough to detect the presence of small and/or low concentrations of secondary phase crystallites. Nevertheless, after eight consecutive redox cycles (Figure 3-d) the Ni (111) reflection had significantly narrowed in the XRD of Ni/LST compared to the reflection after the initial reduction (Figure 3-b), thus indicating the undesired process of Ni crystallite growth. No significant peak narrowing was observed in the case of LSTN.

The fact that Ni was changing oxidation states between that of NiO and of Ni^0 over the course of the redox cycle in the case of Ni/LST, whereas it was changing reversibly between Ni^{n+}_{oct} inside the perovskite and Ni^0 in the case of LSTN, is reinforced by the Ni K-edge X-ray absorption near edge spectra (XANES) of LSTN (Figure 4-a) and Ni/LST (Figure 4-b). The spectrum of the reference Ni-foil showed a clear edge at 8333 eV and no whiteline was visible, which is typical for metallic samples. The absorption edge of NiO was shifted towards higher energies (8340 eV) due to the higher oxidation state of Ni^{2+} and the spectrum included a clear single peak of the whiteline. The spectrum also contained a local minimum at 8361 eV, which can be used as a fingerprint feature of NiO in the Ni K-edge XANES region. The spectrum of calcined LSTN showed a more complex and intense witheline including a shoulder at 8352 eV and no feature at 8361 eV.

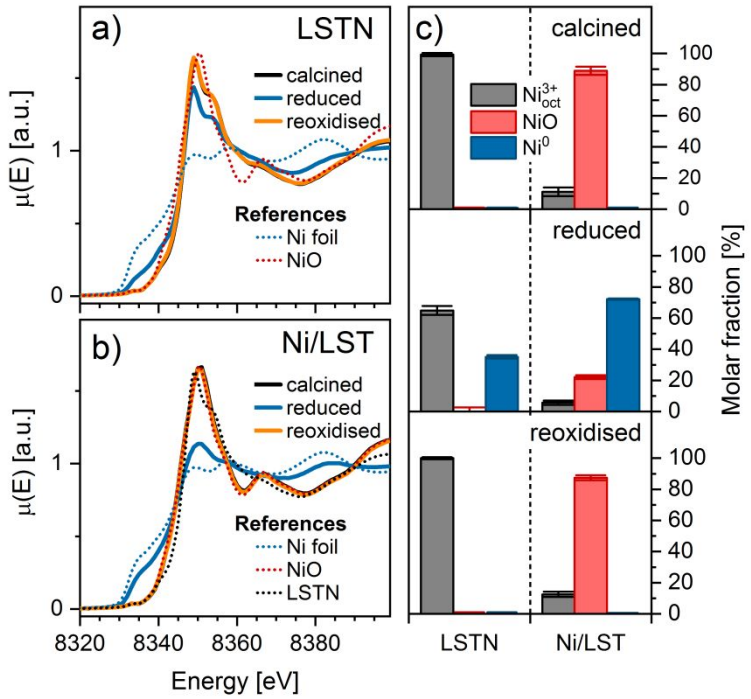

Figure 4. Normalized Ni K-edge (8333 eV) X-ray absorption near edge structure (XANES) data obtained for (a) LSTN and (b) Ni/LST calcined, reduced (10 vol% H_2, 800°C, 1 h) and reoxidised (20 vol% O_2, 800°C, 2 h). The spectra of Ni-foil and NiO reference materials are also shown. c) Ni speciation obtained from linear combination fitting of XANES data on LSTN and Ni/LST after calcination, after reduction and after reoxidation.

The spectra obtained after calcination and reoxidation completely overlapped in both materials. After reduction at 800°C, the spectra exhibited an intensified feature at 8335 eV and a whiteline of decreased intensity, thus resembling a linear combination of the spectra of the calcined material and the Ni-foil reference. Linear combination analysis was performed to determine the contribution of each Ni species (NiO, Ni^0 and Ni^{n+}_{oct}) to the spectra of the reduced materials. The spectrum of LSTN was taken as representative of Ni^{n+}_{oct} Results are presented in Figure 4-c and the full fits and residuals are provided in Figure S3. Nickel was predominantly present as NiO on Ni/LST (>85 %). The coordination of the remaining Ni resembled the one of Ni^{n+}_{oct}, which could indicate possible Ni incorporation into LST.

After reduction at 800°C, 35 % of the overall Ni was reduced to metallic Ni in the case of LSTN, whereas the extent of reduction was much higher (70 %) for impregnated Ni/LST. This behavior is explained with the fact that Ni in LSTN is evenly distributed within the bulk of the perovskite lattice and is not easily accessible to the reducing environment. In the case of Ni/LST, Ni is directly exposed to the gas environment. In both cases reoxidation restored the original Ni species. The observation of the reversible Ni segregation in the case of LSTN validates all observations and interpretations obtained by electron microscopy, XRD and TPR.

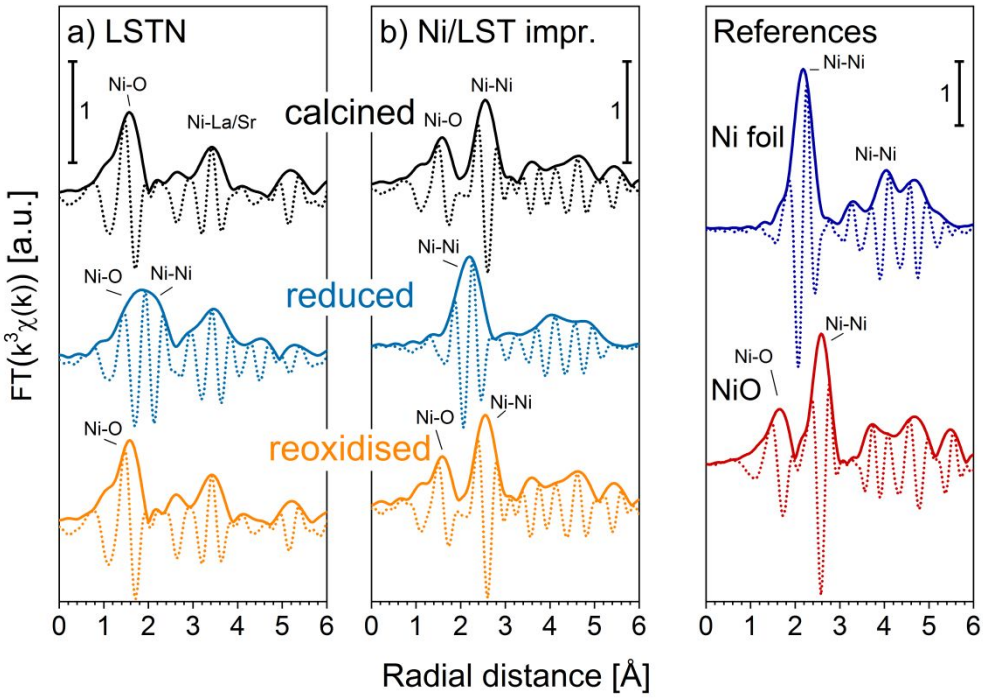

Figure 5. Fourier transformed k^3-weighted Ni K-edge EXAFS data obtained for (a) LSTN and (b) Ni/LST calcined, after reduction (800°C, 10 vol% H_2, 1 h) and reoxidation (800°C, 20 vol% O_2, 2 h). Features are labelled according to their underlying scattering paths. Reference compounds are shown for comparison.

Extended X-ray absorption fine structure (EXAFS) analysis and fitting consolidate our claim of reversible Ni segregation from LSTN. The radial distribution function obtained by Fourier

transformation of the k^3-weighted EXAFS is shown in Figure 5. The signals of all reference materials displayed substantial differences (Figure 5-a). Nickel metal exhibits a characteristic first peak at 2.48 Å corresponding to the first Ni coordination shell, which consists of twelve neighboring Ni atoms in the fcc crystal structure. The first coordination shell of Ni in NiO contains six oxygen anions at a distance of 2.07 Å followed by a Ni coordination shell at 2.95 Å. In LSTN (Figure 5-b) the first oxygen coordination shell was found at a mean distance of 1.95 Å, which is shorter than in NiO due to the higher oxidation state of Ni in LSTN. The second coordination shell at around 3.3 Å is provided by the A-site cations (La^{3+} and Sr^{2+}) while the Ni-Ni feature present in NiO was absent. The development of the feature at 2.5 Å corresponding to the Ni coordination shell in Ni metal was observed after reduction in both LSTN (Figure 5-a) and Ni/LST (Figure 5-b). Upon reoxidation the original coordination environment of Ni was completely restored in both samples, as revealed by the similarity of the radial distribution curves of the reoxidised and the calcined states. Similar conclusions can also be drawn directly from the k^3-weighted EXAFS functions ($k^3 \cdot \chi(k)$, Figure S4) as signature features of each Ni species and coordination state in the samples are clearly visible. The signature features included a distinct triple feature between 5.0 Å and 6.5 $Å^{-1}$ for Ni^{n+}_{oct} in LSTN, where the first two peaks were weak and followed by an intense third feature. The range in wavenumbers used for identification of NiO is somewhat narrower (5.8-6.8 $Å^{-1}$) and included a distinctive double feature, of which the second peak was slightly more pronounced. The complete reversibility of $k^3 \cdot \chi(k)$ profiles between calcined and reoxidised LSTN and Ni/LST can therefore already be appreciated prior to Fourier transformation.

3.3 Redox stability of water gas shift catalyst

The ability of the anode material to catalyze water gas shift (WGS) is widely regarded to be critical for the efficiency of a SOFC operated on syngas feeds as readily oxidizable H_2 fuel is produced.[53] This is also one of the main reasons for the use of high loadings of metallic Ni in Ni/oxide cermet anodes

besides excellent electronic conductivity of metallic Ni. It is clear that the dynamic conditions in the presence of electric current flow through a working SOFC anode cannot be easily replicated by the relatively simple experimental setup used for catalytic tests in plug flow reactors. Nevertheless, such tests provide important information on the intrinsic redox stability of the catalyst.

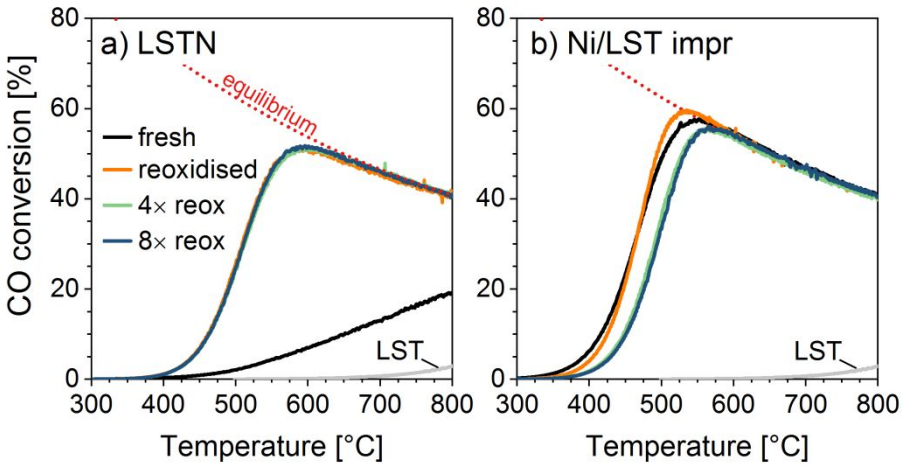

Figure 6. WGS activity profiles of reduced (a) LSTN and (b) Ni/LST over eight redox cycles. Feed gas composition: 15 vol% CO, 15 vol% H_2O, 7.5 vol% H_2, rest Ar; at 30,000 $mLh^{-1}g^{-1}$ (at STP). The calculated theoretical conversion equilibrium is indicated by the dotted red curve.

Figure 6 displays typical CO conversions measured on LSTN (Figure 6-a) and Ni/LST (Figure 6-b) catalysts over eight redox cycles. Pre-reduced LSTN only showed very limited WGS activity and CO conversions did not exceed 20% even at high temperatures under the conditions used in this test. However, after a single oxidation-reduction cycle its catalytic activity improved significantly and equilibrium conversions were reached. It is assumed that this effect arises from increased amounts of Ni made available on the perovskite surface by high temperature reduction. It is obvious that conversion curves of LSTN after four and after eight redox cycles were identical to the one obtained after the first redox cycle. Comparison of the activity of LSTN and Ni/LST to the negligible conversion obtained for Ni-free LST indicated that the Ni metal surface area generated by reduction bestowed

catalytic activity to the material (Figure S5). Stable WGS activity can be regarded as an indication of constant Ni surface area and therefore negligible Ni particle growth over the number of redox cycles. Ni/LST (Figure 6-b) showed maximal conversion already after a single reduction step. This was expected since all Ni is at the surface of the material and available for WGS catalysis on impregnated materials. Redox cycling shifted the conversion curves towards higher temperatures indicating catalytic activity loss, which is likely due to an initial Ni particle growth over the number of redox cycles. However, catalytic activity stabilized after four redox cycles (as documented by SEM in Figure 1). This effect can be related to the decreased driving force of particle sintering as particle growth progresses and/or to the stabilizing nature of the perovskite surface. The evolution of catalytic activity over consecutive redox cycles in both samples demonstrated the particle size stabilizing function of LSTN. Nevertheless, it is worth noticing that the final conversion curve of Ni/LST was still shifted to lower temperatures by around 50°C compared to the one obtained for LSTN after eight redox cycles, likely due to the larger amount of active Ni^0 available on the surface of Ni/LST compared to LSTN as evident from XANES linear combination analysis (Figure 4-c). Since WGS activity is strongly dependent on Ni content, it is not surprising that 60 wt% Ni/YSZ showed the highest activity of all catalysts (Figure S5). Furthermore, redox cycling of Ni/YSZ did not affect catalytic activity towards WGS, which is a consequence of the high Ni content in this sample. However, in a working cell reoxidation of the Ni/YSZ anode can be fatal and leads to mechanical fracture and cell failure due to the extreme volume expansion from Ni to NiO despite the fact that the material may preserve its high catalytic activity.[21] Redox experiments on this material should therefore only be regarded as complementary to the ones performed on the LST-type catalysts.

3.4 Redox stable SOFC anode

Fuel cell tests combined with detailed electrochemical analysis over a number of redox cycles were conducted on full button cells to investigate the performance and stability of LSTN during application as SOFC anode. Figure 7-a shows the current density and cell voltage under various operation conditions for 480 h. Anode reoxidation was carried out nine times, after 21, 24, 27, 45, 48, 51, 190, 194 h and 313 h, respectively, as indicated by vertical dashed time stamp lines. Reoxidation was carried out by a H_2 fuel supply cut-off simulating a gas delivery stop or severe sealing failure. First, the cell was aged for 213 h under open circuit voltage (OCV) conditions (including the first eight redox treatments) before drawing 200 $mAcm^{-2}$ current from the cell under polarization. The polarization resistance development of the cell with time and number of redox cycles was investigated using electrochemical impedance spectroscopy (EIS). In the initial 213 h of the experiment redox stability of the LSTN-CGO material pair was tested by subjecting the cell to eight redox cycles under OCV. The Nyquist plot in Figure 7-b depicts impedance spectra before and after selected redox cycles throughout the thermal aging of the cell. Nyquist plots could be described as "compressed" semicircles indicating the existence of several overlapping processes. In the higher frequency ranges only a minor resistance contribution could be identified. This is mainly attributed to the cathode material, which has an optimized microstructure and long-term stability as demonstrated elsewhere.[54-56] Because the cathode material exhibited a polarization resistance of 0.05 Ωcm^2 in symmetrical cell tests thus contributing only marginally to the overall resistance, all changes in polarization resistance were assigned to the electrochemical processes occurring at the anode. It is important to highlight that the measured ohmic resistance of the cell was very close to the theoretical resistance of the $Sc_{0.12}Zr_{0.88}O_2$ electrolyte and contributions from cell contacts and test rig itself did not affect the measurements. After the first two hours of aging at OCV a rather high area specific resistance (ASR) of 2.46 Ωcm^2 was measured. This high resistance value was attributed to an insufficient reduction and thus limited exsolution of the

catalytically active Ni. Cell performance remarkably improved after 21 h and a first redox cycle, which suggested the exsolution of larger amounts of Ni from bulk LSTN. The redox treatment caused a decrease in ASR to 0.82 Ωcm^2. This behavior reflects the one observed during the catalytic tests on LSTN powders (Figure 6), where the first redox cycle also caused a large increase in catalytic activity indicating substantial increase in active Ni surface area over the first redox cycle.

A further decrease in ASR to 0.71 Ωcm^2 was observed after the following two redox cycles. After 51 h of aging and six redox cycles, the ASR reached 0.60 Ωcm^2, which was four times lower than the initial value measured at the beginning of the experiment. Performance loss accompanied by an ASR increase to 0.77 Ωcm^2 was observed during further aging without redox cycling (OCV, 136 h, 850°C). However, the stimulus of two redox cycles again triggered the materials self-regeneration and led to a performance gain, which resulted in an ASR value of 0.72 Ωcm^2 after 194 h at OCV and eight redox cycles. The analysis of differences in impedance spectra (ADIS), a data evaluation method in EIS, revealed information on the impact of redox cycling on electrochemical performance.[57] A low frequency process in the range of 1-10 Hz (Figure S6) was attributed to the chemical capacitance, which was kinetically limited by the catalytic processes occurring at the surface of the mixed electronic ionic conductor such as LSTN and CGO (i.e. hydrogen oxidation reaction, HOR). Redox cycling, reverse potential mode (-2.0 V), as well as degradation during aging only affected this low frequency domain at 10 Hz, which matches the previous observations. Long-term exposure of LSTN under OCV at 850 °C is expected to cause thermal growth of the Ni particles and hence loss of catalytic activity. In combination with the data from EXAFS and catalytic measurements, it is likely that the redox cycles triggered Ni regeneration. Therefore, the observed variation in the EIS spectra rather reflect the properties of the Ni particles as catalytic active phase in LSTN and is not believed to be related to the additional CGO phase. This claim is supported by the increase in cell performance and decrease of

ASR with successive redox cycles and taking into account higher HOR activity of Ni compared to ceria.[58]

An alternative approach to carry out a redox cycle is to subject the cell to a negative polarization of about -2.0 V (electrolysis mode). The effect of electrolysis on the measured impedance is displayed in Figure 7-c and shows a narrowing of the Nyquist plot and decrease in ASR. ASR decreased to 0.65 Ωcm^2 as oxygen is actively drawn from the anode towards the air electrode at this potential and an oxygen partial pressure of about 10^{-30} Pa is typically reached.[59] This highly reducing atmosphere likely provoked stronger reduction and increased Ni exsolution resulting in larger active Ni surface area and higher performance.

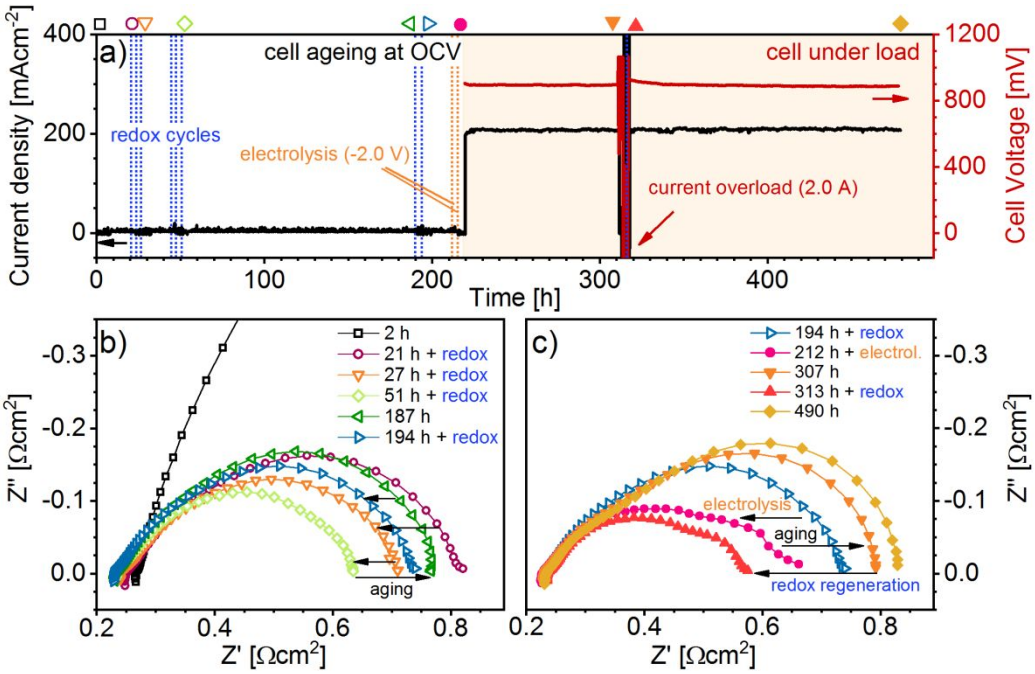

Figure 7. a) Current-Voltage characteristics and an overview of the conditions initiated during the long-term full cell test. White background - open circuit voltage (OCV) conditions, grey background – dynamic conditions with cell polarization. Symbols on top represent the times of EIS corresponding measurements in b) and c). b) Electrochemical impedance spectroscopy data of $La_{0.3}Sr_{0.55}Ti_{0.095}Ni_{0.05}O_3$ – $Ce_{0.9}Gd_{0.1}O_2$ composite electrode operated under OCV conditions. c) Electrochemical impedance spectroscopy data measured for selected condition changes within the dynamic part of the experiment.

After this aging procedure of the cell under OCV conditions, the cell performance was investigated under current load at a total current density of 200 mA·cm^{-2}. The cell test included a period at 313 h (Figure 7-a), when the cell was subjected to severe current overload (2.0 Acm^{-2}). Current overload typically causes a rise in fuel utilization and oxygen partial pressure. It may cause irreversible damage to classical anodes with high Ni content, as Ni may be partially oxidized, similar to a fuel supply interruption.[60] Stability of the cell voltage, remaining practically constant at 890 mV over 255 h under polarization, regardless of the varying conditions, indicates excellent anode stability. Impedance results during this cell operation (Figure 7-c) confirm that anode aging also occurred under current load, as indicated by the increase of ASR from cell test start at 212 h to 307 h from 0.67 Ωcm^2 to 0.79 Ωcm^2 during 90 h of operation at 200 mA·cm^{-2}. However, the cell performance was fully restored by exploiting redox cycling, reversing degradation. Redox cycling was repeated again by interrupting the fuel supply, but also the short period of current overload may have additionally contributed to anode reoxidation. The lowest ASR (0.58 Ωcm^2) for this type of anode was measured after 313 h in combination with this redox cycle. The regeneration of the cell after aging under load demonstrated that the redox stability of the material was also valid under these circumstances.

The electrochemical data clearly shows that LSTN is tolerant to a wide range of potentials and current overloads. It is also clear that redox cycling can be used as an operation strategy to regenerate such anodes and to increase performance characteristics after aging.

3.5 Recovery from sulfur poisoning

Besides offering the possibility for cell operation in electrolysis mode, further potential benefits of the anode redox stability lie in the regeneration from sulfur poisoning, which is a severe problem for cells operated on H_2 feeds.[61] Sulfur poisoning becomes detrimental when WGS catalysis is needed to efficiently convert CO containing fuels.[61] The effect of sulfur on the WGS activity of all catalyst

samples was analyzed by further catalytic tests (Figure 8 and Figure S7). The sulfur recovery was tested after the redox cycles displayed in Figure 6 and Figure S5. After these redox stability tests the sample was treated with 50 ppm of H_2S at 800°C for 2 h under reaction conditions. Finally, CO conversion profiles were recorded after sulfur poisoning and after two further redox (regeneration) cycles. While the already poor activity of Ni-free LST was not affected by the addition of sulfur (Figure S7-b), CO conversions on LSTN and Ni/LST decreased significantly. The sulfur treatment was also sufficient to extinguish the WGS reaction over Ni/YSZ (Figure S7-a) in agreement with the behavior of this anode material in the presence of sulfur.[61] Even though both LSTN (Figure 8-a) and Ni/LST (Figure 8-b) suffered severely from sulfur poisoning, LSTN still retained some activity after poisoning, maintaining 25% CO conversion at 800°C. At this temperature CO conversion of poisoned Ni/LST was as low as 10% and 5% conversion was found on Ni/YSZ. LSTN does not display as much Ni on its surface as either Ni/LST or Ni/YSZ and the fact that it showed the highest activity of the three after poisoning indicates that other WGS active sites than plain Ni^0 may become important, likely as a result of the structural changes induced by Ni segregation.

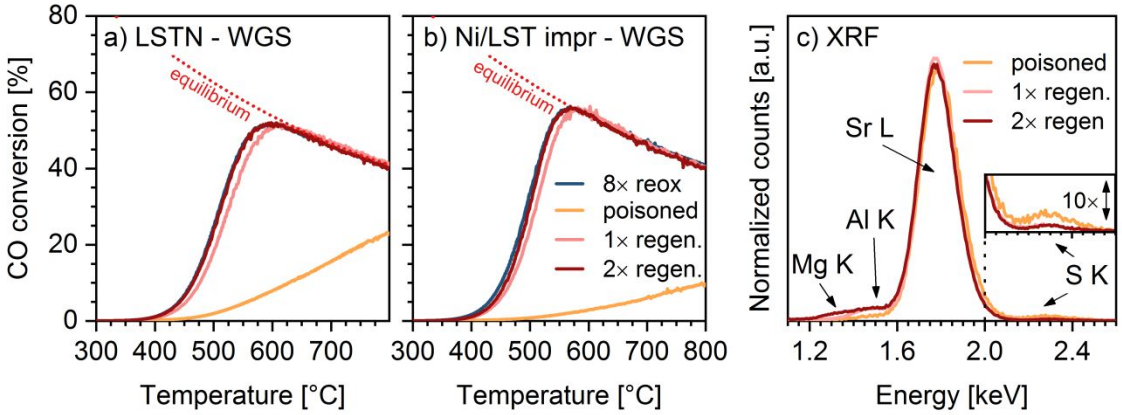

Figure 8. WGS activity profiles of (a) LSTN and (b) Ni/LST after eight redox cycles (prior to poisoning) as well as after H_2S poisoning and two oxidative catalyst regeneration cycles at 800°C. Feed gas composition: 15 vol% CO, 15 vol% H_2O, 7.5 vol% H_2, rest Ar; at 30,000 $mLh^{-1}g^{-1}$ (at STP). The calculated theoretical conversion equilibrium is indicated by the dotted red curve. c) X-ray

fluorescence (1.1 keV – 2.6 keV) obtained on pellet samples of LSTN after H_2S poisoning and after two subsequent oxidative catalyst regeneration cycles at 800°C (2 h oxidation, 1 h reduction). The inset depicts a 10 fold magnification in intensity of the energy range 2.0 keV – 2.6 keV.

Redox cycling of poisoned LSTN, identical to the redox cycling exploited to demonstrate structural reversibility, restored its initial activity. The first regeneration cycle already recovered catalytic activity substantially, whereas a subsequent second regeneration cycle restored the CO conversion to the original levels obtained prior to poisoning. Ni/LST could also be regenerated to a large extent by subjecting it to similar regeneration cycles (Figure 8-b). However, complete regeneration was not achieved. Besides the fact that Ni/YSZ anodes usually cannot be regenerated by redox cycling due to their insufficient redox stability,[21] it is also shown that regeneration of the material used as a catalyst was far from completion even after two regeneration cycles. Fresh Ni/YSZ showed significant activity below 400°C, whereas after sulfur poisoning and two regeneration cycles comparable CO conversion was achieved only at higher temperatures ($\Delta T \sim 50°C$).

Figure 8-c shows X-ray fluorescence (XRF) spectra of LSTN after sulfur poisoning and over two regeneration cycles used to regenerate completely LSTN. Beside Mg K and Al K signals due to the Al sample holder and the presence of traces of the cordierite used to dilute the catalyst bed during catalytic testing, two additional signals could be identified. The Sr L-edge fluorescence signal (1.8 keV) was by far the most prominent while a sulfur K-edge transition was clearly visible at 2.3 keV in the poisoned sample. Despite the intensity decrease already after a single regeneration cycle, sulfur remained detectable after two cycles. Due to the presence of sulfur after catalyst regeneration and the observed complete recovery of WGS activity, it is likely that sulfur traces are deposited on the perovskite surface rather than on the catalytically active Ni and therefore did not interfere with catalytic activity. The exact nature of these species remains unsettled. From the perspective of the Ni phase in the same samples, the Ni K-edge spectra of the poisoned sample, of the sample prior to poisoning (after eight

redox cycles) and after the complete regeneration cycles (reoxidation followed by reduction) overlapped completely (Figure S7). On the other hand, the spectrum of the reoxidised sample resembled the one of calcined LSTN. This clearly indicates that irrespective of sulfur poisoning Ni was able to reincorporate completely during the oxidative treatment of the redox cycle and segregated from the perovskite lattice upon the reductive treatment to restore the catalytically active Ni particles with a sulfur free surface and to regenerate catalytic activity.

4. Conclusions

A redox stable and active Ni based SOFC anode material is presented, which does not make use of precious metals to obtain sulfur tolerance. The cost efficient material exhibits the remarkable property of structural regeneration where Ni can be reversibly exsoluted from the bulk of the perovskite-type mixed oxide through reduction and reincorporated back into the host lattice by reoxidation. The structural reversibility upon redox cycling was documented at microstructure scales as well as on the atomistic level by means of electron microscopy (SEM/TEM/EDX) and with various spectroscopy techniques (EXAFS, XANES, XRD). In addition, the associated reversibility of the catalytic activity was demonstrated by catalytic tests including e.g. WGS activity and TPR profiles. It is shown that Ni exsolution from the perovskite-type host oxide results in the formation of nano scale Ni particles active for the water gas shift reaction, which is important to achieve high efficiencies on fuel cells operated on syngas fuels. Structural reversibility (i.e. the reincorporation of Ni back into the host lattice) can be exploited to regenerate the anode layer after aging, which is known to cause deactivation of current SOFC anodes through Ni particle growth. Redox cycling even activated the $La_{0.3}Sr_{0.55}Ti_{0.95}Ni_{0.05}O_{3-\delta}$ anode material and it was demonstrated that catalytic activity of the material towards the water gas shift reaction could be completely restored after the catalyst had suffered from poisoning by sulfur. It is for the first time that a material with the properties required for SOFC anode applications was

demonstrated to also exhibit the remarkable structural regeneration after sulfur poisoning with the result of a precious metal free, stable and regenerable SOFC anode layer.

5. Acknowledgements

The authors kindly acknowledge the financial support from the Competence Center for Energy and Mobility (CCEM), the Swiss National Science Foundation (SNF, No. 200021_159568). HEXIS AG is thanked for their financial contribution, support and providing fuel cell test facilities. This research project is part of the Swiss Competence Center for Energy Research SCCER BIOSWEET of the Swiss Innovation Agency lnnosuisse. The Swiss Light Source is thanked for the provision of beam times at the SuperXAS and Phoenix I beamlines and Dr. M. Nachtegaal, Dr. C. Borca, Dr. T. Huthwelker and M. Elsener are gratefully acknowledged for their extensive and kind support.

6. Supplementary information

List of catalysts compositions and denotations including primary and secondary crystal phases. XRD patterns of samples after calcination, reduction, reoxidization and reduction after 8 redox cycles. H_2-TPR profiles. Linear combination fit of XANES spectra. k^3-weighted EXAFS spectra. CO conversion profiles of Ni/YSZ and Ni free LST before and after H_2S poisoning. Analysis of Differences in Impedance Spectra (ADIS). Normalized Ni K-edge XANES spectra of LSTN after sulfur poisoning and after regeneration.

6. References

1. Park, S. D.; Vohs, J. M.; Gorte, R. J., Direct oxidation of hydrocarbons in a solid-oxide fuel cell. *Nature* **2000,** *404* (6775), 265-267.

2. Ormerod, R. M., Solid oxide fuel cells. *Chem. Soc. Rev.* **2003,** *32* (1), 17-28.

3. Eguchi, K.; Kojo, H.; Takeguchi, T.; Kikuchi, R.; Sasaki, K., Fuel flexibility in power generation by solid oxide fuel cells. *Solid State Ionics* **2002,** *152*, 411-416.

4. Yi, Y. F.; Rao, A. D.; Brouwer, J.; Samuelsen, G. S., Fuel flexibility study of an integrated 25 kW SOFC reformer system. *J. Power Sources* **2005,** *144* (1), 67-76.

5. Lo Faro, M.; Antonucci, V.; Antonucci, P. L.; Arico, A. S., Fuel flexibility: A key challenge for SOFC technology. *Fuel* **2012,** *102*, 554-559.

6. Dicks, A. L., Advances in catalysts for internal reforming in high temperature fuel cells. *J. Power Sources* **1998,** *71* (1-2), 111-122.

7. Meusinger, J.; Riensche, E.; Stimming, U., Reforming of natural gas in solid oxide fuel cell systems. *J. Power Sources* **1998,** *71* (1-2), 315-320.

8. Baschuk, J. J.; Li, X. G., Carbon monoxide poisoning of proton exchange membrane fuel cells. *Int. J. Energ. Res.* **2001,** *25* (8), 695-713.

9. Weber, A.; Sauer, B.; Muller, A. C.; Herbstritt, D.; Ivers-Tiffee, E., Oxidation of H_2, CO and methane in SOFCs with Ni/YSZ-cermet anodes. *Solid State Ionics* **2002,** *152*, 543-550.

10. Minh, N. Q., Ceramic fuel cells. *J. Am. Ceram. Soc.* **1993,** *76* (3), 563-588.

11. Dees, D. W.; Claar, T. D.; Easler, T. E.; Fee, D. C.; Mrazek, F. C., Conductivity of porous Ni/ZrO_2-Y_2O_3 cermets. *J. Electrochem. Soc.* **1987,** *134* (9), 2141-2146.

12. Atkinson, A.; Barnett, S.; Gorte, R. J.; Irvine, J. T. S.; Mcevoy, A. J.; Mogensen, M.; Singhal, S. C.; Vohs, J., Advanced anodes for high-temperature fuel cells. *Nat. Mater.* **2004,** *3* (1), 17-27.

13. Cassidy, M.; Lindsay, G.; Kendall, K., The reduction of nickel-zirconia cermet anodes and the effects on supported thin electrolytes. *J. Power Sources* **1996,** *61* (1-2), 189-192.

14. Faes, A.; Hessler-Wyser, A.; Zryd, A.; Van herle, J., A review of redox cycling of solid oxide fuel cells anode. *Membranes* **2012,** *2*, 585-664.

15. Madi, H.; Diethelm, S.; Ludwig, C.; Van herle, J., Organic-sulfur poisoning of solid oxide fuel cell operated on bio-syngas. *Int. J. Hydrogen Energ.* **2016,** *41* (28), 12231-12241.

16. Kuhn, J. N.; Lakshminarayanan, N.; Ozkan, U. S., Effect of hydrogen sulfide on the catalytic activity of Ni-YSZ cermets. *J. Mol. Catal. A* **2008,** *282* (1-2), 9-21.

17. Dong, J.; Cheng, Z.; Zha, S. W.; Liu, M. L., Identification of nickel sulfides on Ni–YSZ cermet exposed to H_2 fuel containing H_2S using Raman spectroscopy. *J. Power Sources* **2006,** *156* (2), 461-465.

18. Yang, L.; Cheng, Z.; Liu, M. L.; Wilson, L., New insights into sulfur poisoning behavior of Ni-YSZ anode from long-term operation of anode-supported SOFCs. *Energ. Environ. Sci.* **2010,** *3* (11), 1804-1809.

19. Lussier, A.; Sofie, S.; Dvorak, J.; Idzerda, Y. U., Mechanism for SOFC anode degradation from hydrogen sulfide exposure. *Int. J. Hydrogen Energ.* **2008,** *33* (14), 3945-3951.

20. Malzbender, J.; Wessel, E.; Steinbrech, R. W., Reduction and re-oxidation of anodes for solid oxide fuel cells. *Solid State Ionics* **2005,** *176* (29-30), 2201-2203.

21. Sarantaridis, D.; Atkinson, A., Redox cycling of Ni-based solid oxide fuel cell anodes: a review. *Fuel Cells* **2007,** *7* (3), 246-258.

22. Holzer, L.; Iwanschitz, B.; Hocker, T.; Munch, B.; Prestat, M.; Wiedenmann, D.; Vogt, U.; Holtappels, P.; Sfeir, J.; Mai, A.; Graule, T., Microstructure degradation of cermet anodes for solid oxide fuel cells: quantification of nickel grain growth in dry and in humid atmospheres. *J. Power Sources* **2011,** *196* (3), 1279-1294.

23. Marina, O. A.; Canfield, N. L.; Stevenson, J. W., Thermal, electrical, and electrocatalytical properties of lanthanum-doped strontium titanate. *Solid State Ionics* **2002,** *149* (1-2), 21-28.

24. Tao, S. W.; Irvine, J. T. S., A redox-stable efficient anode for solid-oxide fuel cells. *Nat. Mater.* **2003,** *2* (5), 320-323.

25. Verbraeken, M. C.; Iwanschitz, B.; Mai, A.; Irvine, J. T. S., Evaluation of Ca doped $La_{0.2}Sr_{0.7}TiO_3$ as an alternative material for use in SOFC anodes. *J. Electrochem. Soc.* **2012,** *159* (11), 757-762.

26. Yoo, K. B.; Choi, G. M., Performance of La-doped strontium titanate (LST) anode on LaGaO3-based SOFC. *Solid State Ionics* **2009,** *180* (11-13), 867-871.

27. Boulfrad, S.; Cassidy, M.; Traversa, E.; Irvine, J. T. S., Improving the Performance of SOFC Anodes by Decorating Perovskite with Ni Nanoparticles. *Solid Oxide Fuel Cells 13 (SOFC-XIII)* **2013,** *57* (1), 1211-1216.

28. Neagu, D.; Oh, T. S.; Miller, D. N.; Ménard, H.; Bukhari, S. M.; Gamble, S. R.; Gorte, R. J.; Vohs, J. M.; Irvine, J. T. S., Nano-socketed nickel particles with enhanced coking resistance grown *in situ* by redox exsolution. *Nat. Commun.* **2015,** *6*, 1-8.

29. Jardiel, T.; Caldes, M. T.; Moser, F.; Hamon, J.; Gauthier, G.; Joubert, O., New SOFC electrode materials: the Ni-substituted LSCM-based compounds $(La_{0.75}Sr_{0.25})(Cr_{0.5}Mn_{0.5-x}Ni_x)O_{3-d}$ and $(La_{0.75}Sr_{0.25})(Cr_{0.5-x}Ni_xMn_{0.5})O_{3-d}$. *Solid State Ionics* **2010,** *181* (19-20), 894-901.

30. Burnat, D.; Kontic, R.; Holzer, L.; Steiger, P.; Ferri, D.; Heel, A., Smart material concept: reversible microstructural self-regeneration for catalytic applications. *J. Mater. Chem. A* **2016,** *4* (30), 11939-11948.

31. Arrivé, C.; Delahaye, T.; Joubert, O.; Gauthier, G., Exsolution of nickel nanoparticles at the surface of a conducting titanate as potential hydrogen electrode material for solid oxide electrochemical cells. *J. Power Sources* **2013,** *223*, 341-348.

32. Oh, T. S.; Rahani, E. K.; Neagu, D.; Irvine, J. T. S.; Shenoy, V. B.; Gorte, R. J.; Vohs, J. M., Evidence and model for strain-driven release of metal nanocatalysts from perovskites during exsolution. *J. Phys. Chem. Lett.* **2015,** *6* (24), 5106-5110.

33. Tanaka, H.; Taniguchi, M.; Uenishi, M.; Kajita, N.; Tan, I.; Nishihata, Y.; Mizuki, J.; Narita, K.; Kimura, M.; Kaneko, K., Self-regenerating Rh- and Pt-based perovskite catalysts for automotive-emissions control. *Angew. Chem. Int. Edit.* **2006,** *45* (36), 5998-6002.

34. Nishihata, Y.; Mizuki, J.; Akao, T.; Tanaka, H.; Uenishi, M.; Kimura, M.; Okamoto, T.; Hamada, N., Self-regeneration of a Pd-perovskite catalyst for automotive emissions control. *Nature* **2002,** *418* (6894), 164-167.

35. Kuc, J.; Zhang, Y. C.; Erni, R.; Yoon, S.; Karvonen, L.; Weidenkaff, A.; Matam, S. K., Composition dependent self-regenerative property of perovskite-type oxides. *Phys. Status Solidi RRL* **2015,** *9* (5), 282-287.

36. Eyssler, A.; Winkler, A.; Safonova, O.; Nachtegaal, M.; Matam, S. K.; Hug, P.; Weidenkaff, A.; Ferri, D., On the state of Pd in perovskite-type oxidation catalysts of composition $A(B,Pd)O_{3\pm d}$ (A = La, Y; B = Mn, Fe, Co). *Chem. Mater.* **2012,** *24* (10), 1864-1875.

37. Lai, K.-Y.; Manthiram, A., Self-regenerating Co–Fe nanoparticles on perovskite oxides as a hydrocarbon fuel oxidation catalyst in solid oxide fuel cells. *Chem. Mater.* **2018,** *30*, 2515-2525.

38. Steiger, P.; Delmelle, R.; Foppiano, D.; Holzer, L.; Heel, A.; Nachtegaal, M.; Krocher, O.; Ferri, D., Structural Reversibility and Nickel Particle stability in Lanthanum Iron Nickel Perovskite-Type Catalysts. *ChemSusChem* **2017,** *10* (11), 2505-2517.

39. Deng, J.; Cai, M. D.; Sun, W. J.; Liao, X. M.; Chu, W.; Zhao, X. S., Oxidative methane reforming with an intelligent catalyst: sintering-tolerant supported nickel nanoparticles. *ChemSusChem* **2013,** *6* (11), 2061-2065.

40. Sun, Y. F.; Li, J. H.; Zeng, Y. M.; Amirkhiz, B. S.; Wang, M. N.; Behnamian, Y.; Luo, J. L., A-site deficient perovskite: the parent for in situ exsolution of highly active, regenerable nano-particles as SOFC anodes. *J. Mater. Chem. A* **2015,** *3* (20), 11048-11056.

41. Ravel, B.; Newville, M., ATHENA, ARTEMIS, HEPHAESTUS: data analysis for X-ray absorption spectroscopy using IFEFFIT. *J. Synchrotron Radiat.* **2005,** *12*, 537-541.

42. Marschner, F. M., F. W., In *Applied Industrial Catalysis*, Leach, B. E., Ed. Academic Press: New York, 1983; Vol. 2, p 215.

43. Holzer, L.; Munch, B.; Iwanschitz, B.; Cantoni, M.; Hocker, T.; Graule, T., Quantitative relationships between composition, particle size, triple phase boundary length and surface area in nickel-cermet anodes for solid oxide fuel cells. *J. Power Sources* **2011,** *196* (17), 7076-7089.

44. Faes, A.; Hessler-Wyser, A.; Presvytes, D.; Vayenas, C. G.; Van herle, J., Nickel-zirconia anode degradation and triple phase boundary quantification from microstructural analysis. *Fuel Cells* **2009,** *9* (6), 841-851.

45. Burnat, D.; Ried, P.; Holtappels, P.; Heel, A.; Graule, T.; Kata, D., The rheology of stabilised lanthanum strontium cobaltite ferrite nanopowders in organic medium applicable as screen printed SOFC cathode layers. *Fuel Cells* **2010,** *10* (1), 156-165.

46. Burnat, D.; Heel, A.; Holzer, L.; Otal, E.; Kata, D.; Graule, T., On the chemical interaction of nanoscale lanthanum doped strontium titanates with common scandium and yttrium stabilized electrolyte materials. *Int. J. Hydrogen Energ.* **2012,** *37* (23), 18326-18341.

47. Hjalmarsson, P.; Sun, X. F.; Liu, Y. L.; Chen, M., Influence of the oxygen electrode and inter-diffusion barrier on the degradation of solid oxide electrolysis cells. *J. Power Sources* **2013,** *223*, 349-357.

48. Megaw, H. D., Crystal structure of double oxides of the perovskite type. *Proc. Phys. Soc.* **1946,** *58* (326), 133-152.

49. Tanaka, H.; Tan, I.; Uenishi, M.; Taniguchi, M.; Nishihata, Y.; Mizuki, J., The intelligent catalyst: Pd-perovskite having the self-regenerative function in a wide temperature range. *Key Eng. Mater.* **2006,** *317-318*, 827-832.

50. Mile, B.; Stirling, D.; Zammitt, M. A.; Lovell, A.; Webb, M., The location of nickel-oxide and nickel in silica-supported catalysts - 2 forms of NiO and the assignment of temperature-programmed reduction profiles. *J. Catal.* **1988,** *114* (2), 217-229.

51. Wachsman, E. D.; Lee, K. T., Lowering the temperature of solid oxide fuel cells. *Science* **2011,** *334* (6058), 935-939.

52. Stobbe, E. R.; de Boer, B. A.; Geus, J. W., The reduction and oxidation behaviour of manganese oxides. *Catal. Today* **1999,** *47* (1-4), 161-167.

53. Matsuzaki, Y.; Yasuda, I., Electrochemical oxidation of H_2 and CO in a H_2 - H_2O - CO - CO_2 system at the interface of a Ni-YSZ cermet electrode and YSZ electrolyte. *J. Electrochem. Soc.* **2000,** *147* (5), 1630-1635.

54. Holzer, L.; Iwanschitz, B.; Hocker, T.; Munch, B.; Presta, M.; Wiedenmann, D.; Vogt, U.; Holtappels, P.; Sfeir, J.; Mai, A.; Graule, T., Microstructure degradation of cermet anodes for solid oxide fuel cells: quantification of nickel grain growth in dry and in humid atmospheres. *J. Power Sources* **2011,** *196* (3), 1279-1294.

55. Iwanschitz, B.; Holzer, L.; Mai, A.; Schutze, M., Nickel agglomeration in solid oxide fuel cells: the influence of temperature. *Solid State Ionics* **2012,** *211*, 69-73.

56. Iwanschitz, B.; Sfeir, J.; Mai, A.; Schutze, M., Degradation of SOFC anodes upon redox cycling: a comparison between Ni/YSZ and Ni/CGO. *J. Electrochem. Soc.* **2010,** *157* (2), B269-B278.

57. Burnat, D.; Nurk, G.; Holzer, L.; Kopecki, M.; Heel, A., Lanthanum doped strontium titanate - ceria anodes: deconvolution of impedance spectra and relationship with composition and microstructure. *J. Power Sources* **2018,** *385*, 62-75.

58. Primdahl, S.; Mogensen, M., Mixed conductor anodes: Ni as electrocatalyst for hydrogen conversion. *Solid State Ionics* **2002,** *152*, 597-608.

59. Ye, L.; Zhang, M.; Huang, P.; Guo, G.; Hong, M.; Li, C.; Irvine, J. T. S.; Xie, K., Enhancing CO_2 electrolysis through synergistic control of non-stoichiometry and doping to tune cathode surface structures. *Nat. Commun.* **2017,** *8*.

60. Comminges, C.; Fu, Q. X.; Zahid, M.; Steiner, N. Y.; Bucheli, O., Monitoring the degradation of a solid oxide fuel cell stack during 10,000 h via electrochemical impedance spectroscopy. *Electrochim. Acta* **2012,** *59*, 367-375.

61. Hagen, A., Sulfur poisoning of the water gas shift reaction on anode supported solid oxide fuel cells. *J. Electrochem. Soc.* **2013,** *160* (2), F111-F118.

Table of Content